

Cluster Dynamics with HETDEX - I: Simulated Performance, Mass Distribution and Limits

Steven Boada,¹★ C. Papovich,¹ R. Wechsler,^{2,3} T. S. Li,¹
K. Gebhardt,⁴ E. Rozo,² E. S. Rykoff,²

¹*George P. and Cynthia Woods Mitchell Institute for Fundamental Physics and Astronomy, Texas A&M University, College Station, TX, 77843-4242*

²*Kavli Institute for Particle Astrophysics and Cosmology, Department of Physics, Stanford University, Stanford, CA 94305, USA*

³*Department of Particle Physics and Astrophysics, SLAC National Accelerator Laboratory, Menlo Park, CA 94025, USA*

⁴*The University of Texas*

Accepted XXX. Received YYY; in original form ZZZ

ABSTRACT

The study of clusters of galaxies has been argued to be a very effective way to measure cosmological parameters, including measuring dark energy and testing models of gravity. The Hobby Eberly Telescope Dark Energy Experiment (HETDEX) will observe many hundreds of square degrees, covering a large sample of galaxy clusters out to $z = 0.5$ based on their optical spectra (3500 – 5500Å). The spectra will provide important measures of the clusters dynamics and may enable constraints on cosmological parameters, but only if the measurements provide accurate estimates of the total cluster masses. We have carried out a study to investigate the ability of HETDEX to recover accurate galaxy cluster masses over a wide range of masses and redshifts. We used a detailed mock galaxy catalog and present mock observations of two different scenarios: (1) We targeted individual galaxy clusters to investigate the recovery of parameters with such observations. (2) We created and evaluated a HETDEX-like selection “function” of galaxies over a similarly sized portion of the sky and use well adopted techniques to recover the dynamical properties, such as velocity dispersion and mass. Using both observing strategies, we produce cluster mass probability density functions $P(X|M, z)$, which can be used to determine the probability that a galaxy cluster of given mass (M), located at redshift (z) determined using observable parameter (X).

1 INTRODUCTION

Our ability to perform precision cosmology with clusters of galaxies has reached a critical turning point. The widely accepted Λ CDM model of cosmology makes explicit predictions about the number and masses of galaxy clusters throughout the universe. However, connecting these predictions to a set of, sufficiently large in size, observed clusters remains a principal problem. Specifically, the largest threat to modern, precision, cluster cosmology is not the identification of large numbers of clusters (the total number of clusters known is only going up) but the accurate recovery of galaxy cluster mass (e.g., [Sehgal et al. 2011](#); [Planck Collaboration 2013](#); [Bocquet et al. 2015](#)).

As mass is not a direct observable, a lot of work is underway to characterize galaxy cluster masses with an observable feature of galaxy clusters. The goal is to constrain, as best possible, $P(X|M, z)$ the probability (P) that a galaxy cluster of given mass (M), located at redshift (z) determined using observable parameter (X). The observable parameter most commonly observed X-ray temperatures and luminosities (e.g., [Mantz et al. 2010](#); [Rykoff et al. 2014](#); [Mantz et al. 2015](#)), cosmic microwave background observa-

tions (e.g., [Vanderlinde et al. 2010](#); [Sehgal et al. 2011](#)) using the Sunyaev-Zel’dovich effect (SZE; [Sunyaev & Zeldovich 1972](#)) or optical studies (e.g., [Roza et al. 2010, 2015](#)) of richness (e.g., [Abell 1958](#); [Rykoff et al. 2012](#)) or galaxy velocity dispersions (e.g., [Ruel et al. 2014](#); [Sifón et al. 2015b](#)).

Massive surveys, both on going and planned, are revolutionizing cluster cosmology using a large range of wavelengths. The South Pole Telescope (SPT; [Carlstrom et al. 2011](#)) and the Atacama Cosmology Telescope (ACT; [Swetz et al. 2011](#)) are discovering many clusters through the SZE. Optically, the on going The Dark Energy Survey (DES; [The Dark Energy Survey Collaboration 2005](#)) and planned Large Synoptic Survey Telescope (LSST; [LSST Dark Energy Science Collaboration 2012](#)) will identify many thousands of clusters to much lower masses than is possible with SZE measurements. However, regardless of the discovery method used, spectroscopic followup is needed to further constrain $P(X|M, z)$. But as the cluster dataset grows to many tens of thousands of clusters individual followup becomes increasingly impractical. Therefore, large spectroscopic surveys are needed to more fully constrain the observable–mass relation of clusters.

The Hobby Eberly Telescope Dark Energy eXperiment

(HETDEX; Hill et al. 2008) is a trailblazing effort to observe high-redshift large scale structures using cutting edge wide-field integral field unit (IFU) spectrographs. Designed to probe the evolution of the dark energy equation of state etched onto high redshift ($z > 2$) galaxies by the Baryon Acoustic Oscillations (Eisenstein et al. 2005) in the first moments of the universe, the survey will observe two fields for a total of 420 degree² from two fields (300 degree², Spring field and 120 degree², Fall field). Tuned to find Ly α emitting (LAE) galaxies at $1.9 < z < 3.5$, HETDEX expects to find 800,000 LAEs, and more than one million [O II] emitting galaxies at $z < 0.5$ masquerading as high-redshift galaxies (Acquaviva et al. 2014).

While a large portion of the $\sim 10^6$ interloping [O II] galaxies will be field (not associated with a bound structure) galaxies, the large area covered by HETDEX is expected to contain as many as 100 Virgo-sized ($M_{\text{dyn}} \sim 10^{15} M_{\odot}$) clusters at $z < 0.5$ (citation?). The near-complete spectroscopic coverage allows an unprecedentedly detailed look at a very large number of clusters ranging from group scales to the very massive. In addition to the recovery of accurate dynamical masses, detailed investigations of the of dynamical state of the clusters is possible.

Connecting the dynamical properties derived from spectroscopy to the properties inferred from other studies insures the greatest impact on future work. HETDEX overlaps with the Sloan Digital Sky Survey (SDSS; Blanton et al. 2001), SDSS stripe 82 (Annis et al. 2014), the Dark Energy Survey (DES; The Dark Energy Survey Collaboration 2005), and the upcoming DECam/IRAC Galaxy Environment Survey (DIRGES; PI: Papovich, C. Papovich et al. in preparation). **SHELA and others? Would be good to have a whole list of different things and different wavelengths.** While the potential dataset is very rich, two large issues remain.

It is unclear how a blind spectroscopic survey with an IFU will effect the recovery of galaxy cluster dynamical properties. Unlike many previous large cluster surveys (e.g., Milvang-Jensen et al. 2008; Robotham et al. 2011; Sifón et al. 2015b) which use multi-object spectrographs, the Visible Integral-Field Replicable Unit Spectrograph (VIRUS; Hill et al. 2012) used by HETDEX samples the sky unevenly which could excluded member galaxies which would otherwise be included. Secondly, it is not straightforward to use spectroscopic redshifts predominately from emission-line galaxies to interpret the kinematic and dynamical states of the clusters.

This work plans to address these concerns in the following ways. We use simulated observations which target individual galaxy clusters to investigate the recovery of parameters with such observations. Secondly, we create and evaluate a HETDEX like selection “function” of galaxies over a similarly large portion of the sky and use well adopted techniques to recover the dynamical properties, such as velocity dispersion and mass. Each observation strategy will further be constrained with “ideal” and “realistic” knowledge. Ideal knowledge assumes that we know which individual galaxy is assigned to which cluster. With realistic knowledge this is unknown and must be determined prior to the estimation of the cluster properties. Both of these strategies will better allow future work to predict the number and types of galaxy clusters which should be observed with VIRUS during both

the HETDEX survey portion and through targeted follow up observations.

Give outline of paper section.

Throughout this paper, we adopt the following cosmological model ($\Omega_{\Lambda} = 0.77$, $\Omega_M = 0.23$, $\sigma_8 = 0.83$ and $H_0 = 72 \text{ km s}^{-1} \text{ Mpc}^{-1}$), assume a Chabrier initial mass function (IMF; Chabrier 2003), and use AB magnitudes (Oke 1974).

2 DATA AND MOCK OBSERVATIONS

Blah blah intro stuff... Lorem ipsum dolor sit amet, consectetur adipiscing elit, sed do eiusmod tempor incididunt ut labore et dolore magna aliqua. Ut enim ad minim veniam, quis nostrud exercitation ullamco laboris nisi ut aliquip ex ea commodo consequat. Duis aute irure dolor in reprehenderit in voluptate velit esse cillum dolore eu fugiat nulla pariatur. Excepteur sint occaecat cupidatat non proident, sunt in culpa qui officia deserunt mollit anim id est laborum.

2.1 The “Buzzard” Catalogs

The “Buzzard” mock galaxy catalogs (R. Wechsler et al., private communication) cover 375.68 degree² between $60 < RA < 90$ and $-61 < DEC < -41$ and are derived from a combination of Sub-halo Abundance Matching (ShAM) and ADDSEDs (Adding Density Dependent Spectral Energy Distributions) tied to an in house n-body cosmological simulation. A brief description of the catalog creation is described as follows. The initial conditions are generated with a second-order Lagrangian perturbation theory using 2LP-Tic (Crocce et al. 2006). Dark matter (DM) n-body simulations are run using LGadget-2 (a version of Gadget-2; Springel 2005). The DM halos are identified using the ROCKSTAR halo finder (Behroozi et al. 2013) which also calculates halo masses and other various parameters.

Galaxy M_r luminosities are added to the velocity peaks using ShAM (Reddick et al. 2013), and ADDSEDs (Adding Density Dependent Spectral Energy Distributions) assign luminosities in the other bands. A M_r -density-SED relation is created using a SDSS training set, and for each mock galaxy the SED of a randomly selected training set galaxy which has a similar M_r and density is assigned. The result is a 398.49 sq. degree mock catalog occupying a $60 \leq RA \leq 90$ and $-40 \leq DEC \leq -61$ portion of the sky. It contains 238 million galaxies with $r \text{ mag} < 29$ and $z \leq 8.7$.

The catalog information, used in this study, is broken into two large portions. The “truth” files contain the characteristics of each individual galaxies, such as right ascension (RA), declination (DEC), redshift (z), observed and rest-frame magnitudes, and many others. The “halo” files contain information for individual halos, to which many individual galaxies may belong. This includes five estimations of dynamical mass, RA, DEC, z , three dimensional velocity dispersion, and many others.

However, the catalogs do not include information on emission or absorption lines or estimations of whether the halo is relaxed or not. We supplement the catalogs with this information and describe the method in Section 2.2 and others.

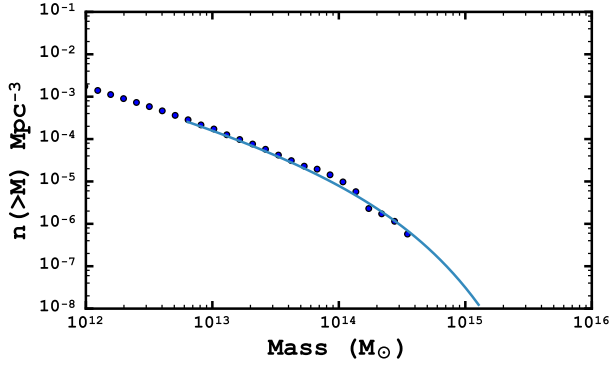


Figure 1. The cumulative MF (from Tinker et al. 2008) of halos above M_{200c} at $z = 0.1$

We investigate the accuracy of the halo mass distribution by comparing the cumulative number density of halos above a mass (M_{200c}) threshold to the halo mass function (HMF) of Tinker et al. (2008). Shown in Figure 1 the HMF is calculated at central redshifts of 0, 0.2, and 0.4 using `HM-Fcalc` (Murray et al. 2013) and compared to galaxies in a redshift window of $\Delta z \pm 0.01$. We find a very good agreement between the expected HMF and the observed.

2.2 [O II] Luminosity

The Buzzard “truth” catalog does not provide [O II] luminosities so we must assign them empirically. We use 503113 galaxies from the SDSS Data Release 12 (Alam et al. 2015) from $z = 0.05 - 0.2$, which are selected with no redshift warning, and place each galaxy on a color-magnitude diagram (CMD) of M_r and $g - r$, see Figure 2.

To assign an [O II] luminosity to each galaxy in our catalog we place the catalog galaxies on the same CMD and select all SDSS galaxies in a small 2D (M_r , $g - r$) bin around the galaxy. We extract all of the SDSS galaxies inside that bin and create a histogram of their [O II] luminosities. Using a slice sampling technique (Neal 1997) we assign the catalog galaxy an [O II] luminosity based on the distribution of SDSS galaxies extracted. For catalog galaxies which are placed on the CMD near no, or very few ($1 \leq n < 10$) galaxies we assign it zero [O II] luminosity or the mean luminosity, respectively.

The right panel of Figure 2 shows the CMD of all SDSS galaxies. Two potential catalog galaxies are also placed on the CMD (M_r , $g - r = -17.7, 0.49$ and M_r , $g - r = -21.4, 1.24$) and indicated by two colored boxes. The histograms shown in the Figure’s left panel shows the probability density histograms of the Log [O II] luminosity for the SDSS galaxies in the 2D bin. We sample the distribution and assign each catalog galaxy an [O II] luminosity which is then converted into a flux.

2.3 Mock Observations

Not sure this does a good enough job talking about the two different observations. Tentatively slated to start in the spring of 2016, HETDEX will perform blind spectroscopy

($R \sim 750$ in $3500 - 5500 \text{ \AA}$) over two fields along the celestial equator. The 300 degree^2 , spring field and 120 degree^2 , fall field will have no preselected targets. Using VIRUS on the 10-m Hobby-Eberly Telescope (HET; Ramsey et al. 1998) the completed survey is expected to have an overall fill-factor of $1/4.5$, meaning that the entire area could be covered with 4.5 dithers of the entire survey.

The spectral coverage allows for the detection of [O II] ($\lambda\lambda 3727 - 3729 \text{ \AA}$ doublet) emitters to $z \sim 0.5$ and Ca H ($\lambda 3968.5 \text{ \AA}$) and K ($\lambda 3933.7 \text{ \AA}$) absorption features to $z \sim 0.4$. HETDEX is expected to detect sources with continuum brighter than 22 mag in g , and emission line strengths above $3.5 \times 10^{-17} \text{ erg s}^{-1} \text{ cm}^{-2}$. So we “observe” $z < 0.4$ galaxies which meet either the emission line or the magnitude limit. Galaxies $0.4 < z < 0.5$ are only observed if their emission line strength is sufficient. **These limits have been changed. FIX!**

In this work we consider two separate observation cases. The first are targeted observations where we select each galaxy cluster and “observe” each galaxy within $8'$ of the center. The second is a survey case where observations which are blind to the positions of the clusters are conducted. In both cases, our “observations” consist of placing masks down onto the Buzzard “truth” catalogs and selecting all, $z < 0.5$ also meeting sensitivity limits, galaxies which lie underneath. Each mask is created to accurately reproduce the HETDEX IFU pattern, see Figure 3. The pattern consists of 78 IFUs, which are comprised of 448 optical fibers subtending a $50'' \times 50''$ region on the sky (Kelz et al. 2014). The inter-IFU spacing is also $50''$ spanning a total area of $16' \times 16'$ on the sky.

The individual IFUs have a fill-factor of $1/3$, which will be completely filled with three dithers of the telescope at each pointing. This means that when selecting galaxies from the Buzzard catalog we assume an observation for all galaxies laying within a colored, IFU square in Figure 3. **This should be updated with the fiber collisions.** Galaxies which lie between the IFUs are missed, as well as the galaxies which lie between the pointings, as there is no overlap between one pointing and the next. To cover the 375.67 degree^2 field of the Buzzard catalog we require 5370 pointings where 0.015 degree^2 of each pointing is covered by an IFU. The total area of the sky covered by an IFU is 80.80 degree^2 which gives a filling factor of $1/4.65$ slight decreased from the expected filling factor of $1/4.5$.

3 RECOVERY OF PARAMETERS

In the following sections, we outline the methods we use to derive the dynamical properties of the galaxy clusters in our sample. This is not meant to be an exhaustive study of the different methods used to recover these parameters. The following is, in many cases, a subset of the available methods to derive any single parameter. The specific choice of method may improve or diminish the accuracy of the recovered parameter, but the methods chosen were to facilitate comparison with observational studies.

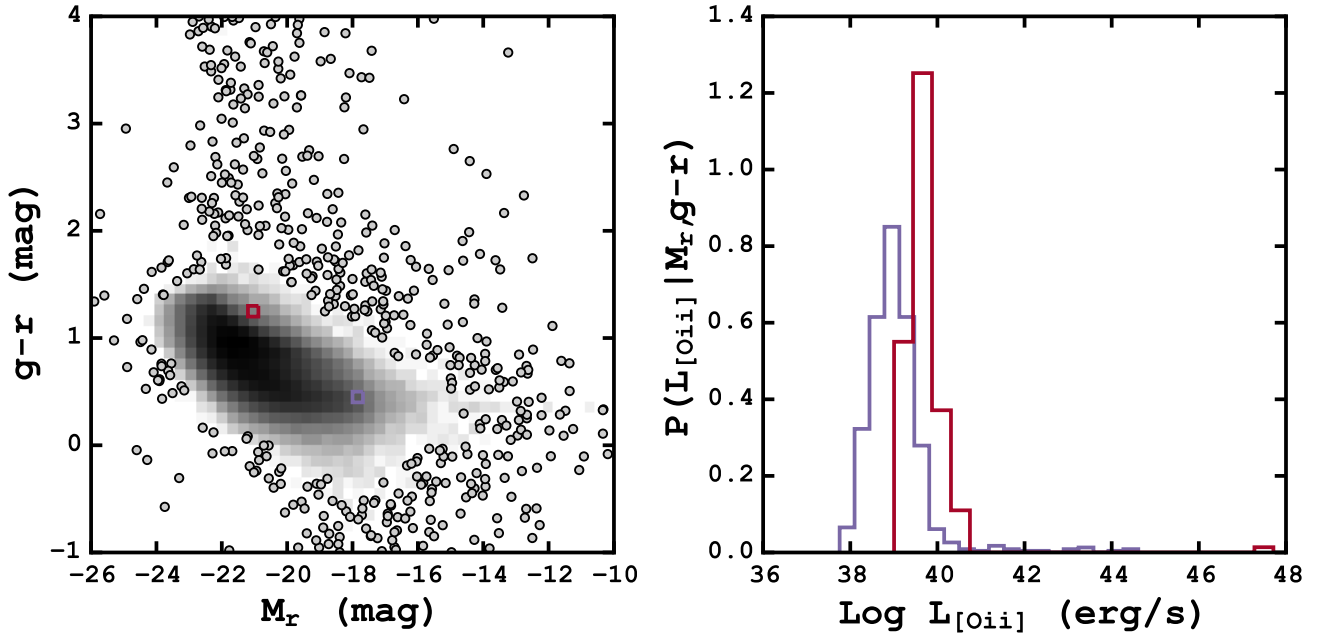


Figure 2. *Left:* CMD of 503113 $z < 0.2$ galaxies take from the SDSS DR12 where the shading scales with the density of points. The two boxes show regions containing potential catalog galaxies. *Right:* Probability histograms of the Log [O II] luminosity for the SDSS galaxies located in the two highlighted regions on the right. New [O II] luminosity (and subsequently fluxes) are assigned to catalog galaxies from slice sampling the probability histogram.

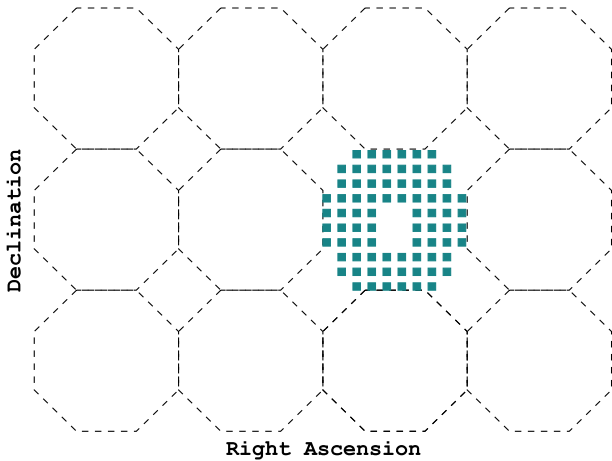


Figure 3. Representative observation tiling scheme for the HETDEX $16' \times 16'$ pointings. Each colored square is a single VIRUS IFU and the dashed octagons approximate the size of a single observation. See the text for more details.

3.1 Cluster Redshift

The accurate determination of the cluster redshift (z_c) is crucial to the reliability of all following measurements. An incorrect cluster redshift introduces errors into the measured line-of-sight velocity (LOS v) and corresponding dispersion, which, in turn, contributes to errors associated with dynamical mass and radius.

In simple terms, the cluster redshift is the mean of the

redshifts of all galaxies associated with the cluster. However, because the standard mean can be quite sensitive to outliers or otherwise contaminated data, we require a more resistant statistic, and turn to the biweight location estimator (Beers et al. 1990) which provides improved performance.

3.2 Line-of-Sight Velocity Dispersion

We first calculate the line-of-sight velocity (LOS v) to each galaxy, where

$$LOSv = c \frac{z - z_c}{1 + z_c} \quad (1)$$

and c is the speed of light in km s^{-1} , z is the redshift of the individual galaxy, and z_c is the overall cluster redshift described in the previous section.

The line-of-sight velocity dispersion (LOS v D) is calculated using a method of maximum likelihood following Walker et al. (2006). We maximize the probability function

$$p(v_1, \dots, v_N) = \prod_{i=1}^N \frac{1}{\sqrt{2\pi(\sigma_i^2 + \sigma_p^2)}} \exp\left[-\frac{1}{2} \frac{(v_i - \langle \mu \rangle)^2}{(\sigma_i^2 + \sigma_p^2)}\right] \quad (2)$$

where σ_p , $\langle \mu \rangle$, and σ_i is the LOS v D, the average radial velocity and the error on the individual LOS v s respectively. Using a Monte Carlo Markov Chain (MCMC) sampler (emcee¹; Foreman-Mackey et al. 2013), we draw twenty thousand samples from the posterior probability distribution. Simple priors, $\langle \mu \rangle$ lies between the maximum and minimum

¹ <http://dan.iel.fm/emcee/current/>

LOSVD and $0 < \sigma_p$ **check**, are used. When the full distribution of LOSVDs are not used, the final LOSVD is quoted as the median value of the posterior probability distribution with 68% error bars defined as the 16th and 84th percentiles of the same distribution.

In principle, a single statistic such as the biweight scale estimator or the gapper estimator (both from [Beers et al. 1990](#)) with many bootstrap resamplings could be used to construct a distribution of σ_p . In simple tests where the values of both σ_p and $\langle \mu \rangle$ are known. The 68% error bars derived from the MCMC method give slightly better results with the true LOSVD value bracketed by the error bars in $\sim 68\%$ of the cases versus $\sim 57\%$ with bootstrapping and a single statistic. In addition, we prefer the maximum likelihood method for its straight forward treatment of the errors in the LOSVD measurements.

3.3 Dynamical Mass

Recently, the relationship between the LOSVD and dynamical mass has been the focus of several studies (e.g., [Evrard et al. 2008](#); [Saro et al. 2013](#); [Sifón et al. 2013](#); [van der Burg et al. 2014](#)), and a best fitting relationship for the mass enclosed by r_{200c} of the form

$$M_{200c} = \frac{10^{15}}{h(z)} \left(\frac{\sigma_{1D}}{A_{1D}} \right)^{1/\alpha} M_{\odot} \quad (3)$$

with $A_{1D} = 1177 \pm 4.2 \text{ km s}^{-1}$ ([Munari et al. 2013](#); referred to as σ_{15} in [Evrard et al. 2008](#) and other works), $\alpha = 1/3$, $h(z) = H(z)/100$, and σ_{1D} is the LOSVD of the velocity tracers (dark matter particles, subhalos or galaxies).

A growing body of work suggests that there is a significant difference in the observed LOSVD depending on the velocity tracers used. Specifically, while there is little difference between using galaxies and their host DM subhalos, there is a significant over estimation of the LOSVD when using galaxies/subhalos compared to DM particles ([Munari et al. 2013](#)). We follow other works (e.g., [Kirk et al. 2015](#); [Sifón et al. 2015a](#)) using the scaling relation, given in Equation 3 from [Munari et al. \(2013\)](#) to facilitate comparisons with other observational studies.

3.4 Dynamical Mass Corrections

In this section we use two methods to predict the mass of a cluster based on other observables. Often the cluster mass is estimated based on a single observable, X-ray temperature, velocity dispersion, richness and others. Here we combine many observables to attempt to correct the mass inferred solely from the velocity dispersion. The first method is traditional probability based where we marginalize over a series of observables to find the most probable mass. The second is based on a machine learning (ML) algorithm which attempts to “learn” the relationship between the observables and the desired output, the mass. Both of these methods are examples of supervised learning algorithms where the relationship between the observable (known) parameters and the target parameter (the mass) are both known.

As with any predictive analysis it is important to test the model on data that the model has not seen before. In this section we take all of the observed clusters, our full sample,

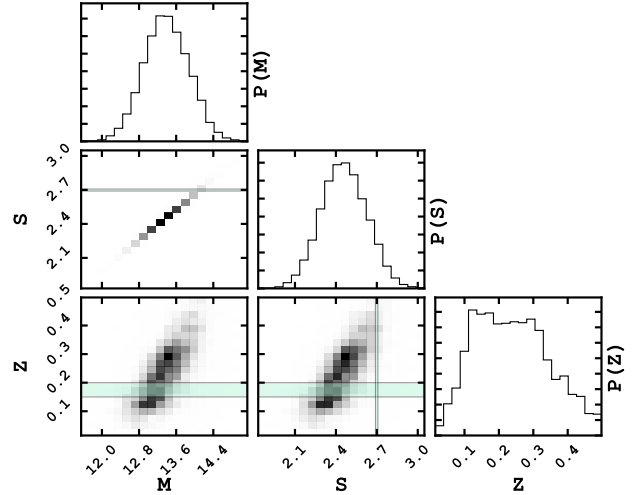


Figure 4. Corner plot of the *training* data with features σ and z . The corner plots shows all of the one and two dimensional posterior probability distributions used to determine the correct cluster mass. The colored rectangles show the slices needed to create a conditional probability distribution of the mass, $P(M|\vec{x})$. See text for a complete description.

split them, and generate a training and testing set. The data is randomly split 70% training and 30% testing. We follow the ML convention and refer to the individual clusters in each set as a “sample”, and the parameters associated with the cluster (z , LOSVD, mass, etc.) as “features”.

3.4.1 Probability Based

We begin with the training sample. After selecting the desired features $\vec{x} = \{\sigma, z, \dots\}$ we make the joint probability between the true cluster mass (M) and \vec{x} . Because \vec{x} can be multidimensional, we rely on the corner plot to visualize the relationship between all of the training features. Figure 4 shows all of the one (marginalized probability) and two (joint probability) dimensional projections of the posterior probability distributions of the features of the training data.

The conditional probability of the mass $P(M|\vec{x} = \{x_1, x_2, \dots\})$ is determined by taking a slice through the joint probability distributions in bins centered on the desired value. The slices show by the colored bars in Figure 4 are centered on $\sigma = 500 \text{ km s}^{-1}$ and $z = 0.17$. The distribution of mass contained in the three dimensional bin given by the intersection of these slices is $P(M|\vec{x} = \{\sigma = 500 \text{ km s}^{-1}, z = 0.17\})$.

For the clusters making up the *test* sample the mass is unknown (it is what we are trying to predict) but the other features are known. To determine the mass probability distribution of a test cluster, $P(M)$ we combine the conditional probability distribution, $P(M|\vec{x})$, created previously with the probability distribution of σ through Equation 4.

$$P(M) = \int P(M|\vec{x})P(\sigma)d\sigma \quad (4)$$

The expected mass is determined by integrating the mass

probability, $P(M)$ over all mass. This becomes our “predicted” mass, $\langle M \rangle$.

$$\langle M \rangle = \int M' P(M') dM' \quad (5)$$

The confidence interval associated with this prediction can be estimated two ways. First, by calculating the variance about the expected mass through

$$V = \int (M' - \langle M \rangle)^2 P(M') dM' \quad (6)$$

or by drawing many samples from $P(M)$ and calculating the values at the 16th and 84th percentile. In practice we find that both methods produce similar results for a large number of trials. Therefore, we quote predicted masses as the most probable mass given by Equation 5 and associated 68% error estimated through Equation 6.

3.4.2 Machine Learning Based

The estimation in this section relies on a ML technique known as an ensemble method, where many estimators are created by a single learning method with the goal of improved generalization and robustness compared to a single estimation. Ensemble methods come in two general flavors. Averaging methods average (hence the name) the estimators to produce a single prediction. Boosting estimators build estimates sequentially by attempting to address poor performing estimators in each previous step, hence “boosting” the predictive power.

Here we use an averaging ensemble learning method known as a forest of randomized decision trees often shorten to just random forest (RF). Decision trees can be visualized a flow chart where forks are the branches of the tree. The path along the tree is decided by the values of the feature at each branch. RF estimators use a random subset of the training set at each fork to decide which path should be followed. The final prediction is then the average of all the trees. We use RF regression methods as implemented in *Scikit-Learn* (Pedregosa et al. 2012).

Any uncertainties quoted by this method are, in fact, prediction intervals. A prediction interval is an estimate of the interval encompassing future observations, with a certain probability. And, unlike confidence intervals, which describe certainties on the different moments of a population, a prediction interval is unique to each prediction. In many regression analyses, such as linear fitting, the prediction intervals are based on underlying assumptions of normally distributed residuals. However, RF estimators do not have any such assumptions and require special treatment.

The prediction intervals here are based on the general method of quantile regression forests (Meinshausen 2006).

The 68% prediction interval is determined by calculating the 16th and 84th percentile of all the predictions made by the ensemble of estimators. **should talk about how random forests can give error bars on the individual estimates.**

4 RESULTS

Here we explore the cluster member recovery rate and mass estimates for the two observing strategies. We discuss the

accuracy of dynamical mass derived from both the scaling relation (see Equation 3) and through the probability and ML methods.

4.1 Recovery of Cluster Members

As discussed in Section 2.3 the observational constraints place limits on the total number of cluster member galaxies expected to be recovered. Knowing these limits will provide important information for potential future follow up or targeted observations.

Figure 5 shows the recovery fraction of member galaxies, the number of observed galaxies divided by the number of actual galaxies (N_{obs}/N_{true}), as function of both redshift and cluster mass. It is important to note that if fewer than five member galaxies are observed the cluster is not considered detected, and is excluded from this figure. As expected, the targeted observing strategy where the individual clusters are targeted through several dithers to ensure near complete coverage, performs significantly better than the survey observing strategy across all redshifts and cluster masses.

For the clusters recovered as a function of redshift, there are two effects at work. The decrease in recovery fraction with increasing redshift is a magnitude effect. If, instead of being limited to 22 mag in g -band, the observations were limited by absolute magnitude, the sharp downward trend disappears. The second key feature is the strong decline in clusters recovered from survey observations. This is due to gaps in the VIRUS IFU. The median recovery fraction in survey observations is almost exactly 4.5 times less than the targeted median recovery fraction. As the total filling factor of the survey increases the two lines will converge.

The recovery rate as a function of cluster mass, right panel of Figure 5, shows that of the low mass clusters we detect ($N_{obs} > 5$), observe the majority of the galaxies. This also shows a rapid decrease in the detection fraction, which can again be explained by considering absolute magnitudes instead of apparent magnitudes. Just as before, if the survey was limited by absolute magnitude, we find a much more consistent detection fraction.

4.2 Mass estimates

In this section we discuss how accurately we are able to reproduce the true cluster mass from a set of observations. We report on two methods the probability based approach (Section 3.4.1) and the machine learning based method (Section 3.4.2). For each method we consider both targeted and HETDEX-like observing strategies.

All of the figures presented here show the predicted versus true cluster masses for one of the two observing strategies. In each panel the solid black line shows the 1:1 relationship, the colored, solid line is the median recovered mass, and the shaded region is the 68% scatter of the cluster masses. The lower panels show the fractional mass error:

$$\epsilon = (M_{pred} - M)/M \quad (7)$$

where M_{pred} is the predicted cluster mass and M is the true cluster mass.

Any scatter in recovered masses can be attributed to both physical and numerical effects. As the cluster mass increases, clusters become more virialized and contain many

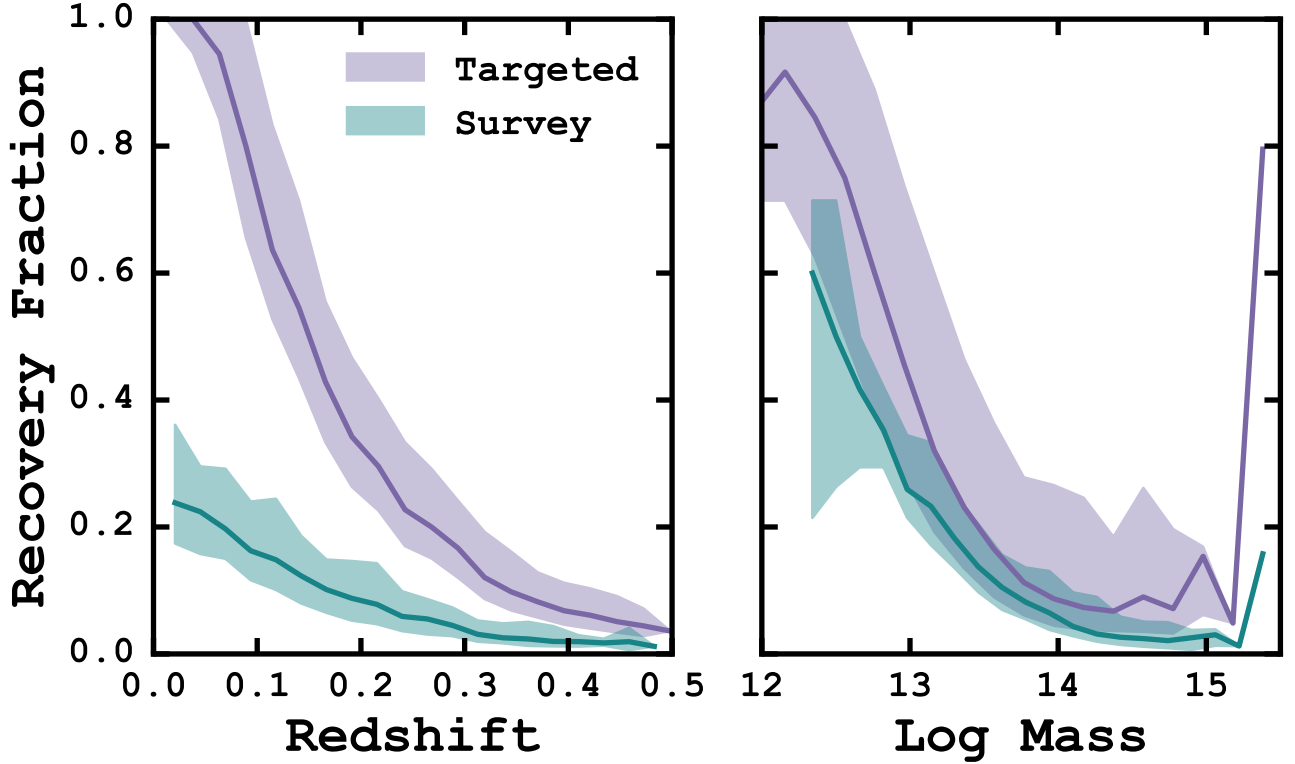


Figure 5. Recovery fractions (N_{obs}/N_{true}) of cluster member galaxies as a function of redshift and mass for the targeted and survey observing strategies. The solid lines are the median values and the shaded regions represent the 68% scatter. The significant decline in galaxies observed with the survey strategy is due to gaps in the VIRUS IFU.

individual galaxies. The presence of any in-falling matter onto lower mass clusters can introduce a significant amount of substructure, which can increase the observed LOSVD increasing the predicted mass. Also, as the number of cluster galaxies decreases the LOSVD PDF is poorly sampled leading to poorly recovered cluster masses due to numerical effects. The masses presented here are recovered using the best possible conditions, where we have perfect knowledge of the cluster membership. In reality, the mass recovery levels presented in this section represent a lower bound on the accuracy achievable through this method. [Ntampaka et al. \(2015\)](#) does have a discussion about how well they do with contaminated galaxy catalogs. We could do something similar and have a similar discussion, but I'm not sure it is worth it. Should be simple enough to do with the targeted catalog, but with the HETDEX catalog it would be pretty bad IMO. We should also talk about how often the true mass lies within the error bars. Many of them are going to be with the 68% range, but we can drop the error estimates to 0.5σ if that actually means anything

4.2.1 Probability Based

Figures 6 and 7 show the power law predictions compared to the predictions based on probability propagation.

Need to talk about the cluster rotations to fill out the

survey data. Otherwise there aren't that many clusters detected.

4.2.2 Machine Learning Based

Figures 8 and 9 show the power law predictions compared to the RF predictions using LOSVD (σ) combined with both z and the number of galaxies observed, N_{gal} .

5 HETDEX AS A GALAXY CLUSTER SURVEY

5.1 Expected Results

Lorem ipsum dolor sit amet, consectetur adipiscing elit, sed do eiusmod tempor incididunt ut labore et dolore magna aliqua. Ut enim ad minim veniam, quis nostrud exercitation ullamco laboris nisi ut aliquip ex ea commodo consequat. Duis aute irure dolor in reprehenderit in voluptate velit esse cillum dolore eu fugiat nulla pariatur. Excepteur sint occaecat cupidatat non proident, sunt in culpa qui officia deserunt mollit anim id est laborum.

5.2 Potential Improvements

Lorem ipsum dolor sit amet, consectetur adipiscing elit, sed do eiusmod tempor incididunt ut labore et dolore magna

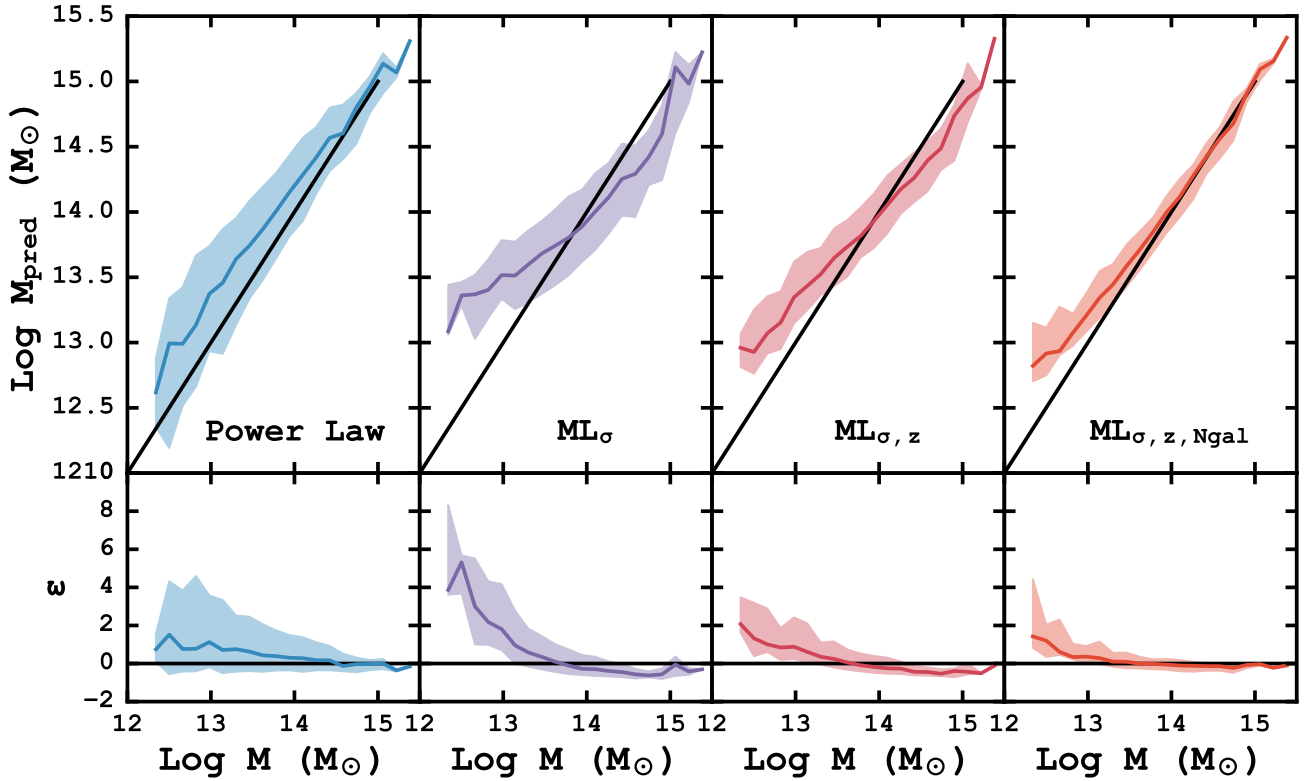


Figure 6. Mass predictions for the power law scaling relation (Equation 3) and the ML technique with different input features. The bottom row of panels shows the fractional error (Equation 7) as a function of mass. The solid black line shows the 1:1 relation. The colored lines and shaded region show the median value and 68% bounds respectively.

aliqua. Ut enim ad minim veniam, quis nostrud exercitation ullamco laboris nisi ut aliquip ex ea commodo consequat. Duis aute irure dolor in reprehenderit in voluptate velit esse cillum dolore eu fugiat nulla pariatur. Excepteur sint occaecat cupidatat non proident, sunt in culpa qui officia deserunt mollit anim id est laborum.

5.3 Extendability to Other Surveys

Lorem ipsum dolor sit amet, consectetur adipisicing elit, sed do eiusmod tempor incididunt ut labore et dolore magna aliqua. Ut enim ad minim veniam, quis nostrud exercitation ullamco laboris nisi ut aliquip ex ea commodo consequat. Duis aute irure dolor in reprehenderit in voluptate velit esse cillum dolore eu fugiat nulla pariatur. Excepteur sint occaecat cupidatat non proident, sunt in culpa qui officia deserunt mollit anim id est laborum.

6 SUMMARY

Lorem ipsum dolor sit amet, consectetur adipisicing elit, sed do eiusmod tempor incididunt ut labore et dolore magna aliqua. Ut enim ad minim veniam, quis nostrud exercitation ullamco laboris nisi ut aliquip ex ea commodo consequat. Duis aute irure dolor in reprehenderit in voluptate velit esse

cillum dolore eu fugiat nulla pariatur. Excepteur sint occaecat cupidatat non proident, sunt in culpa qui officia deserunt mollit anim id est laborum.

ACKNOWLEDGEMENTS

The authors also wish to thank the anonymous referee whose comments and suggestions significantly improved both the quality and clarity of this work. We also thank Steven W. Crawford for many helpful discussions. This research made use of This research made use of the IPython package (Perez & Granger 2007) and matplotlib, a Python library for publication quality graphics (Hunter 2007). Funding for the SDSS and SDSS-II has been provided by the Alfred P. Sloan Foundation, the Participating Institutions, the National Science Foundation, the U.S. Department of Energy, the National Aeronautics and Space Administration, the Japanese Monbukagakusho, the Max Planck Society, and the Higher Education Funding Council for England. The SDSS Web Site is <http://www.sdss.org/>. The SDSS is managed by the Astrophysical Research Consortium for the Participating Institutions.

REFERENCES

Abell G. O., 1958, *ApJS*, 3, 211

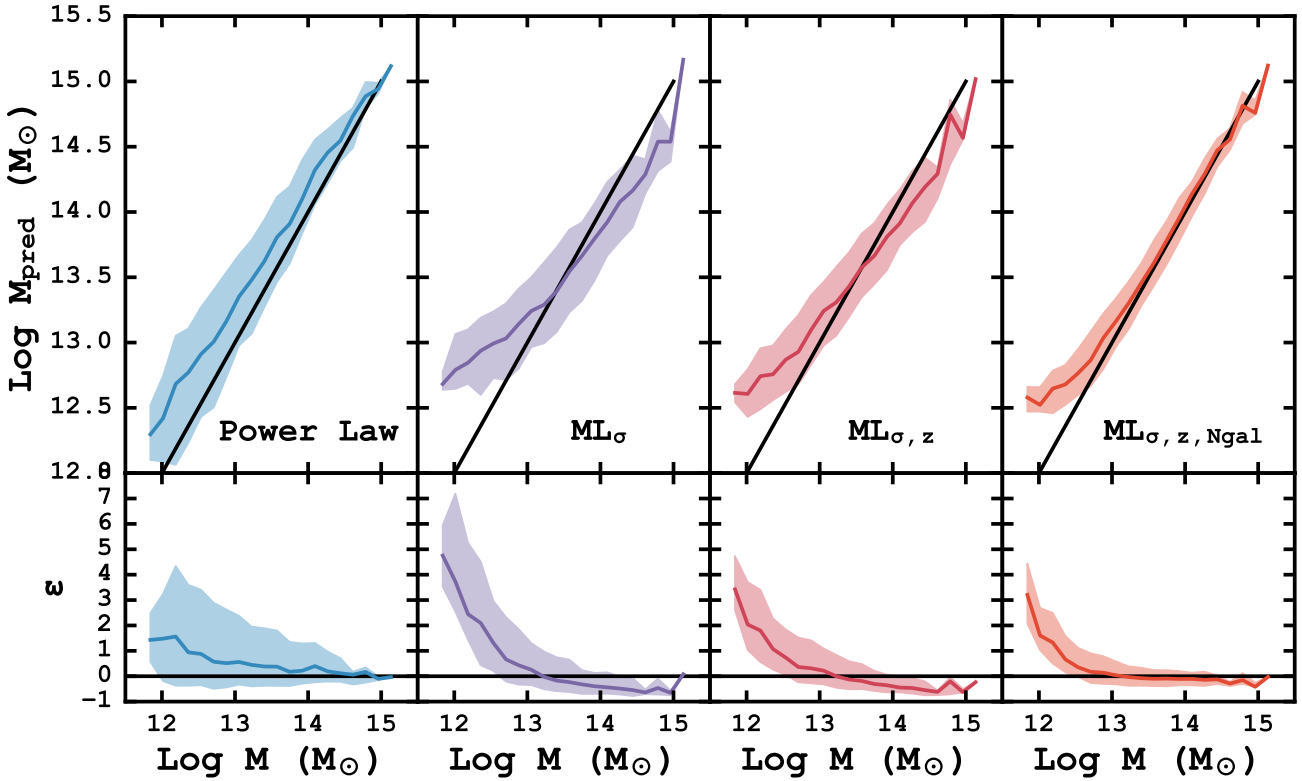


Figure 7. Mass predictions for the power law scaling relation (Equation 3) and the ML technique with different input features. The bottom row of panels shows the fractional error (Equation 7) as a function of mass. The solid black line shows the 1:1 relation. The colored lines and shaded region show the median value and 68% bounds respectively.

Acquaviva V., Gawiser E., Leung A. S., Martin M. R., 2014, *Proc. IAU*, 10, 365
 Alam S., et al., 2015, *ApJS*, 219, 12
 Annis J., et al., 2014, *ApJ*, 794, 120
 Beers T. C., Flynn K., Gebhardt K., 1990, *AJ*, 100, 32
 Behroozi P. S., Wechsler R. H., Wu H.-Y., 2013, *ApJ*, 762, 109
 Blanton M. R., et al., 2001, *AJ*, 121, 2358
 Bocquet S., et al., 2015, *ApJ*, 799, 214
 Carlstrom J. E., et al., 2011, *PASP*, 123, 568
 Chabrier G., 2003, *PASP*, 115, 763
 Crocce M., Pueblas S., Scoccimarro R., 2006, *MNRAS*, 373, 369
 Eisenstein D. J., et al., 2005, *ApJ*, 633, 560
 Evrard A. E., et al., 2008, *ApJ*, 672, 122
 Foreman-Mackey D., Hogg D. W., Lang D., Goodman J., 2013, *PASP*, 125, 306
 Hill G. J., et al., 2008, *Panor. Views Galaxy Form. Evol. ASP Conf. Ser.*, 399
 Hill G. J., et al., 2012, in McLean I. S., Ramsay S. K., Takami H., eds, Vol. 8446, *Ground-based Airborne Instrum. Astron. IV. Proc. SPIE*. p. 84460N, doi:10.1117/12.925434, <http://adsabs.harvard.edu/abs/2012SPIE.8446E..0NH>
 Hunter J. D., 2007, *Comput. Sci. Eng.*, 9, 90
 Kelz A., et al., 2014, in Ramsay S. K., McLean I. S., Takami H., eds, Vol. 9147, *Proc. SPIE*. p. 914775, doi:10.1117/12.2056384, <http://adsabs.harvard.edu/abs/2014SPIE.9147E..75K>
 Kirk B., et al., 2015, *MNRAS*, 449, 4010
 LSST Dark Energy Science Collaboration 2012, *arXiv Prepr. arXiv1211.0310*, p. 133
 Mantz A., Allen S. W., Rapetti D., Ebeling H., 2010, *MNRAS*,

406, no
 Mantz A. B., Allen S. W., Morris R. G., Schmidt R. W., von der Linden A., Urban O., 2015, *MNRAS*, 449, 199
 Meinshausen N., 2006, *J. Mach. Learn. Res.*, 7, 983
 Milvang-Jensen B., et al., 2008, *A&A*, 482, 419
 Munari E., Biviano A., Borgani S., Murante G., Fabjan D., 2013, *MNRAS*, 430, 2638
 Murray S., Power C., Robotham A., 2013, *Astron. Comput.*, 3-4, 23
 Neal R. M., 1997, Technical report, *Markov Chain Monte Carlo Methods Based on ‘Slicing’ the Density Function*. Department of Statistics, University of Toronto, Toronto, doi:10.1.1.48.886
 Ntampaka M., Trac H., Sutherland D. J., Battaglia N., Póczos B., Schneider J., 2015, eprint arXiv:1509.05409
 Oke J. B., 1974, *ApJS*, 27, 21
 Pedregosa F., et al., 2012, *J. Mach. Learn. Res.*, 12, 2825
 Perez F., Granger B. E., 2007, *Comput. Sci. Eng.*, 9, 21
 Planck Collaboration 2013, *A&A*, 571, 19
 Ramsey L. W., et al., 1998, in *Proc. SPIE*. pp 34–42, doi:10.1117/12.319287, <http://adsabs.harvard.edu/abs/1998SPIE.3352...34Rhttp://proceedings.spiedigitallibrary.org/proceeding.aspx?articleid=945060>
 Reddick R. M., Wechsler R. H., Tinker J. L., Behroozi P. S., 2013, *ApJ*, 771, 30
 Robotham A. S. G., et al., 2011, *MNRAS*, 416, 2640
 Rozo E., et al., 2010, *ApJ*, 708, 645
 Rozo E., Rykoff E. S., Bartlett J. G., Melin J.-B., 2015, *MNRAS*, 450, 592
 Ruel J., et al., 2014, *ApJ*, 792, 45

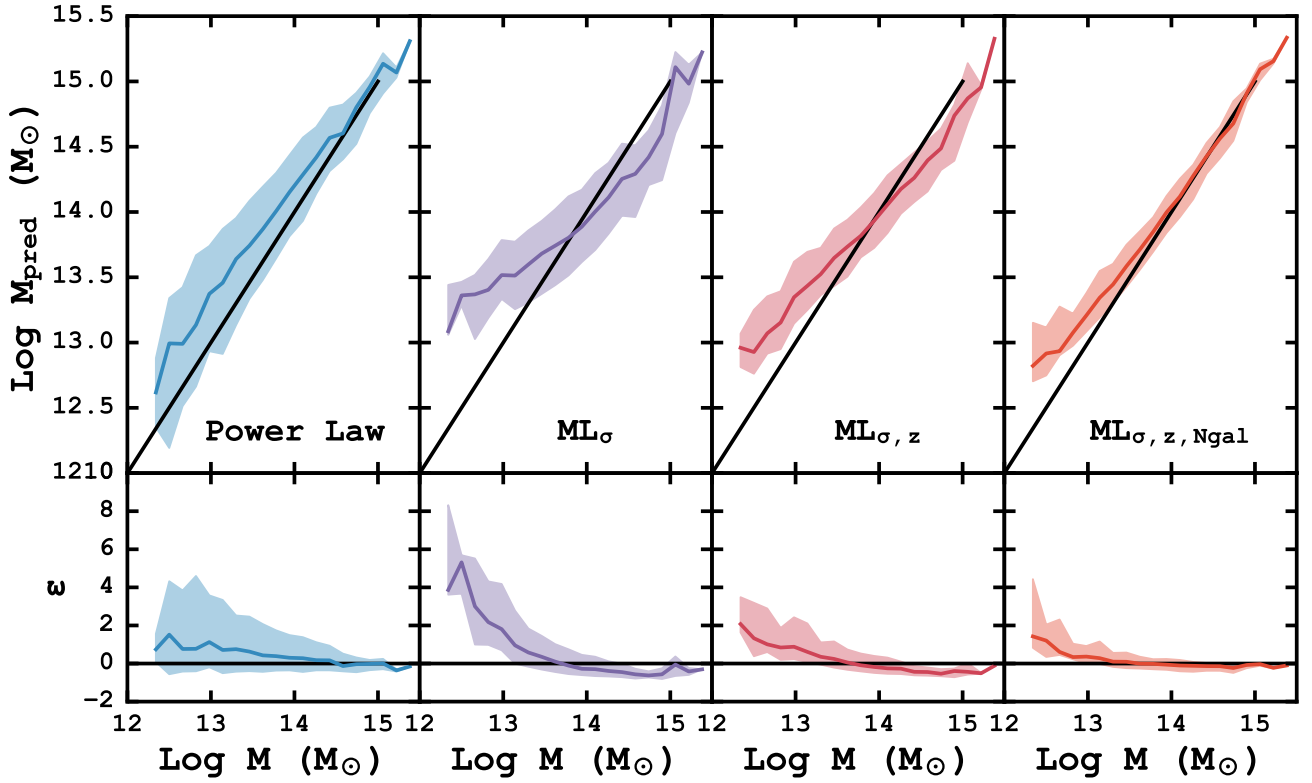


Figure 8. Mass predictions for the power law scaling relation (Equation 3) and the ML technique with different input features. The bottom row of panels shows the fractional error (Equation 7) as a function of mass. The solid black line shows the 1:1 relation. The colored lines and shaded region show the median value and 68% bounds respectively.

- Rykoff E. S., et al., 2012, *ApJ*, 746, 178
 Rykoff E. S., et al., 2014, *ApJ*, 785, 104
 Saro A., Mohr J. J., Bazin G., Dolag K., 2013, *ApJ*, 772, 47
 Sehgal N., et al., 2011, *ApJ*, 732, 44
 Sifón C., et al., 2013, *ApJ*, 772, 25
 Sifón C., et al., 2015a
 Sifón C., Hoekstra H., Cacciato M., Viola M., Köhlinger F.,
 van der Burg R. F. J., Sand D. J., Graham M. L., 2015b,
A&A, 575, A48
 Springel V., 2005, *MNRAS*, 364, 1105
 Sunyaev R. A., Zeldovich Y. B., 1972, *Comments Astrophys. Sp.*
Phys., 4
 Swetz D. S., et al., 2011, *ApJS*, 194, 41
 The Dark Energy Survey Collaboration 2005, eprint arXiv:astro-
 ph/0510346, p. 42
 Tinker J., Kravtsov A. V., Klypin A., Abazajian K., Warren M.,
 Yepes G., Gottlöber S., Holz D. E., 2008, *ApJ*, 688, 709
 Vanderlinde K., et al., 2010, *ApJ*, 722, 1180
 Walker M. G., Mateo M., Olszewski E. W., Bernstein R., Wang
 X., Woodroffe M., 2006, *AJ*, 131, 2114
 van der Burg R. F. J., Muzzin A., Hoekstra H., Wilson G., Lidman
 C., Yee H. K. C., 2014, *A&A*, 561, A79

This paper has been typeset from a $\text{T}_{\text{E}}\text{X}/\text{L}^{\text{A}}\text{T}_{\text{E}}\text{X}$ file prepared by the author.

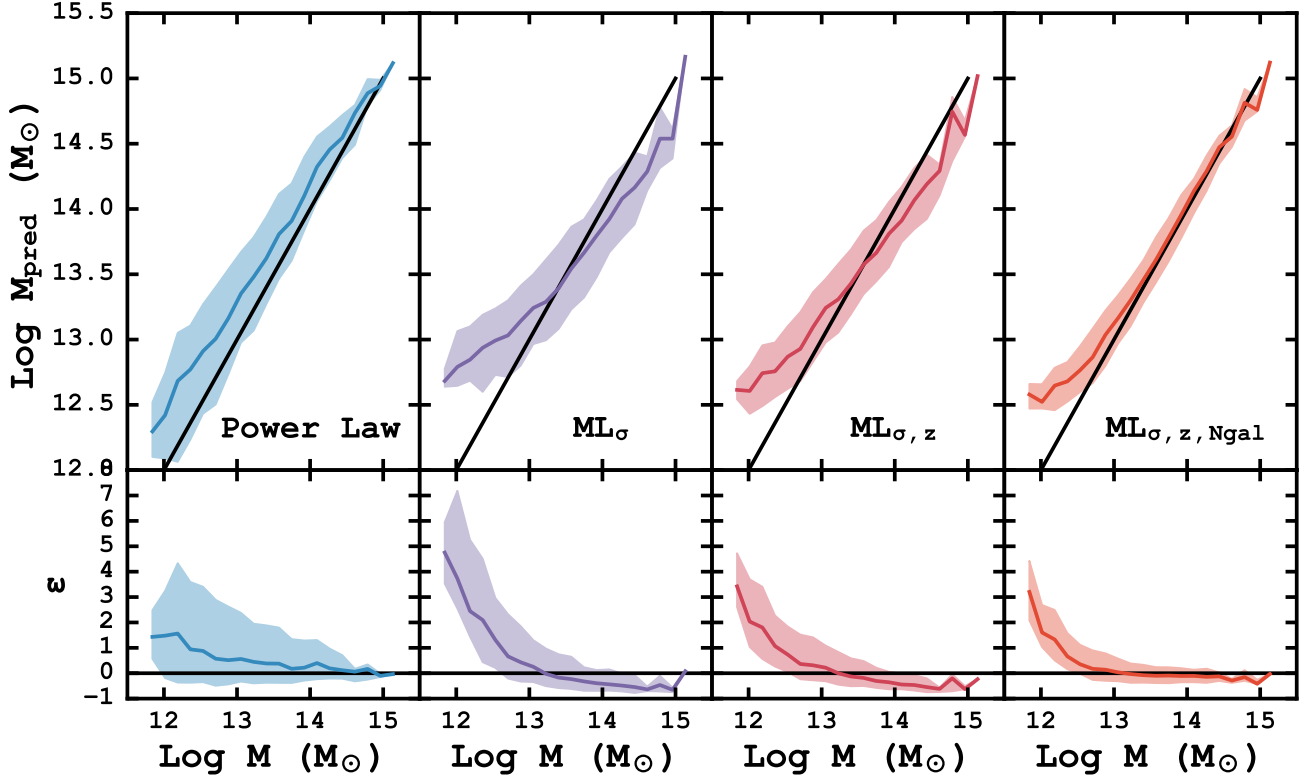


Figure 9. Mass predictions for the power law scaling relation (Equation 3) and the ML technique with different input features. The bottom row of panels shows the fractional error (Equation 7) as a function of mass. The solid black line shows the 1:1 relation. The colored lines and shaded region show the median value and 68% bounds respectively.